

Analysis of Surface Thermal Behavior in Different Local Climate Zones (LCZ): A Case Study in Bragança (Portugal) (2013-2024)

Cátia Rodrigues de Almeida^{1,2,3} ^a, Artur Gonçalves³ ^b and Ana Cláudia Teodoro^{1,2} ^c

¹Department of Geosciences, Environment and Land Planning, Faculty of Sciences, University of Porto,
Rua Campo Alegre, 687, 4169-007 Porto, Portugal

²Earth Sciences Institute (ICT), Pole of the FCUP, University of Porto, 4169-007 Porto, Portugal

³CIMO, LA SusTEC, Institut
up201600831@fc.up.pt, ajg@ipb.pt, amteodor@fc.up.pt 00 253 Bragança, Portugal

Keywords: Urban Heat Island (UHI), Surface Urban Heat Island (SUHI), Remote Sensing (RS), Albedo, Land Use and Land Cover (LULC), Land Surface Temperature (LST).

Abstract: The Urban Heat Island (UHI) effect occurs when temperatures in urban areas are higher than surrounding vegetated areas, especially during the sunset and sunrise. UHI impacts include effects on public health and well-being, changes to the local microclimate, and influence on the local biome. This study evaluates the Land Surface Temperature (LST) and the corresponding Surface Urban Heat Island Intensity (SUHI_{int}) across different Local Climate Zones (LCZs) in Bragança (Portugal) from 2013 to 2024, using images from Landsat 8 and 9 data collected with a portable thermal camera on different surfaces to assess thermal behavior across different scales. The results confirm the existence of the UHI effect in Bragança, where vegetated areas exhibit milder temperatures compared to built areas, especially in summer afternoons. Satellite-derived LST data indicate that the lowest temperature was recorded in an LCZ with vegetation, reaching (-7°C), while the highest minimum temperature was observed in an LCZ with higher density of anthropogenic elements (-3°C). Thermal camera measurements showed that surfaces such as asphalt and exposed soil reached 80 °C in the morning and remained above 60°C in the afternoon. These findings underscore the importance of considering mitigation measures, such as increasing vegetation in urbanized areas or replacing impervious surfaces.


1 INTRODUCTION


The viability of human life in each location requires a series of adaptations in Land Use and Land Cover (LULC), presenting a contemporary challenge. With the global population expected to increase from 7.7 billion to 9.7 billion by 2050 (ONU, 2019), it is essential to pay attention to the surface materials incorporated in the construction of houses, railways, commerce, industry, etc. (Oke, 1987; Weng, 2003). Urbanization can contribute to the formation of the Urban Heat Island (UHI) effect, characterized by higher temperatures in urbanized areas compared to surrounding rural areas (Imhoff *et al.*, 2010; Oke, 1982). A specific approach to this phenomenon is the Surface Urban Heat Island (SUHI), which assesses temperature differences based on temporal variability


and surface characteristics (Voogt & Oke, 2003; Weng & Fu, 2014).

SUHI occurs mainly due to the characteristics of anthropogenic elements in the urban landscape, such as asphalt, sidewalks, and streets (Oke, 1988). These materials have a low albedo, meaning they reflect less solar radiation and retain more heat (Coakley, 2003). Figure 1 shows some materials found in an urban context, along with their respective albedo rates. As observed, most anthropogenic materials exhibit low reflectance.

Beyond albedo, the Local Climate Zones (LCZ) methodology was developed to classify urban and rural environments based on the local landscape and physical and thermal characteristics, such as land cover, terrain structure, building density, surface materials. LCZs are divided into various categories:

^a  <https://orcid.org/0000-0003-4455-9407>

^b  <https://orcid.org/0000-0002-4825-6692>

^c  <https://orcid.org/0000-0002-8043-6431>

on one hand, built zones (urban), including blocks of buildings and residential areas with little or no vegetation, and on the other, natural zones (rural), such as forests, parks, water surfaces, etc. (Errea *et al.*, 2023; Stewart & Oke, 2012).



Figure 1: The albedo of urban materials (adapted from (EPA - United States Environmental Protection Agency, n.d.)).

Remote Sensing (RS) is a methodology applied to understand UHI using data collected by thermal sensors placed on various platforms. The sensors record the electromagnetic radiation emitted or reflected by surfaces without physical contact with the sampled surface, enabling the calculation of Land Surface Temperature (LST) (Pachêco, 2001; Weng *et al.*, 2004). The satellite mission most commonly used for LST calculation, with freely available data distribution, is Landsat, which has included a thermal sensor since Landsat 4 (operational from July 1982 to June 2001) to Landsat 9 (launched in September 2021) (Almeida *et al.*, 2021; US Geological Survey, n.d.-a; Zhou *et al.*, 2019). In addition to satellite data, portable thermal cameras with in situ data collection can complement the methodology, allowing for a more detailed analysis of surface reflectance.

The objective of this study is to evaluate the UHI effect in Bragança (Portugal) using LST data from Landsat 8 and 9 between 2013 and 2023, along with LST data from a portable thermal camera collected during five field campaigns between 2023 and 2024, divided into summer and winter, to assess the seasonal influence on the results.

The choice of Bragança is based on: i) its mountainous setting, which naturally influences wind circulation and speed, potentially contributing to UHI formation; ii) centralized urban densification with surrounding vegetated areas; iii) its classification into seven distinct LCZs, facilitating the understanding of its LULC; and iv) as a supplement to the existing literature, as Bragança's UHI has already been analyzed using RS images and compared with Air Temperature (Ta) data from a monitoring network

with 23 weather stations distributed across seven LCZs between June 29, 2013, and July 5, 2021. In summer, the correlations were strong and very strong, while in winter, they were very strong in all sensors, confirming similar thermal behavior in both parameters (Almeida *et al.*, 2022, 2023; Menezes, 2017).

Our hypothesis is that the integration of RS data acquired by satellites and thermal cameras can confirm the identification of the UHI effect in Bragança and inspire other researchers to implement similar approaches, contributing to the advancement of knowledge and promoting discussions on the need for sustainable urban planning, including the adoption of high albedo materials and green infrastructure to mitigate the UHI effect (Nations, n.d.). The LST measured by satellites and thermal cameras differs in specificity, with expected errors due to spatial resolution and ground proximity. Landsat 8 and 9 sensors acquire LST at 100m, resampled to 30m, limiting the detection of small transition areas. Additionally, the altitude difference reduces atmospheric influences on ground-level data, as thermal cameras capture at 1.5m, while satellites operate from 705 km.

2 METHODOLOGY

2.1 Study Area

Located in the northeastern of Portugal (41°48'20" N, 6°45'42" W), the municipality of Bragança has an area of approximately 1,174 km² and, according to the last census conducted in 2021, has a population of 35,341 inhabitants (Bragança, n.d.; INE, n.d.) (Figure 2). It is a region with complex terrain, significant variability in elevation, and heterogeneous LULC, featuring urban covers, agriculture, forested areas, exposed soils, and natural and vegetated areas. Its economy primarily focuses on public sector service companies (Gonçalves *et al.*, 2018).

Bragança is characterized by a Mediterranean climate, with dry summers and mild temperatures (Csb), as defined in the Köppen-Geiger scale (Barceló & Nunes, 2009). Two scales influence the climate: i) regional, with the atmospheric circulation present in transitional zones (between the ocean and continents); and ii) a more detailed scale, influenced by terrain and proximity to water bodies (lakes or rivers). There are two main rivers in and around Bragança: Fervença (which crosses the region) and Sabor, which is located in a peripheral area and has

less local influence (Bragança, n.d.; Gonçalves *et al.*, 2018).

One of the environmental actions implemented in Bragança is the extensive and continuous collection of temperature and relative humidity data through TGP-4500 model sensors, TinyTag, Gemini Data Loggers, Chichester, UK, installed three meters above the ground, enclosed in a protective white box, semi-leveled on light poles, and oriented towards the South.

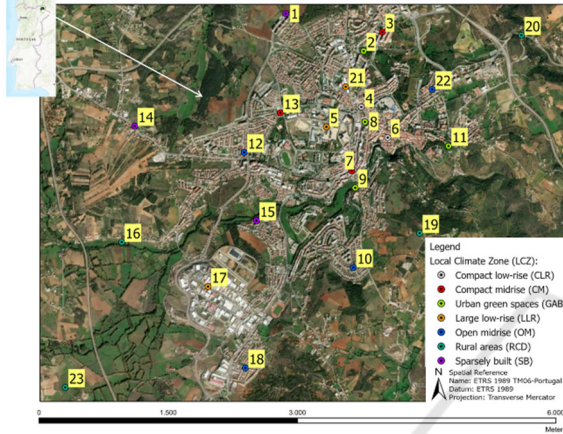


Figure 2. Identification of the 23 Sensors used in this study in Bragança, Portugal: Compact low-rise (CLR) (gray); Compact midrise (CM) (red); Urban green spaces (GAB) (light green); Large low-rise (LLR) (orange); Open midrise (OM) (blue); Rural areas (RCD) (green); Sparsely built (SB) (purple); (adapted from (Almeida *et al.*, 2022)).

The installation criterion for the sensors considered the different LCZs identified in Bragança, ensuring at least three sensors in each class, namely: i) Compact low-rise (CLR): historical city center, including buildings with high density, medium-low height, and presence of embedded bricks/stones (sensors 4 and 6); ii) Compact midrise (CM): modern high-density buildings, with paved surfaces and medium-high height (sensors 3, 7, and 13); iii) Urban green spaces (GAB): predominantly green, covered by trees and low vegetation (sensors 2, 8, 9, and 11); iv) Large low-rise (LLR): industrial and commercial area, with paved parking lots, low or medium density, featuring low and high buildings (sensors 5, 17, and 21); v) Open midrise (OM): streets with isolated or low houses, of medium density (sensors 10, 12, 18, and 22); vi) Sparsely built (SB): transition between rural and urban environments, with scattered houses in forested and agricultural areas (sensors 1, 14, and 15); and vii) Rural areas (RCD): isolated rural spaces surrounding the city (sensors 16, 19, 20, and 23) (Almeida *et al.*, 2022; Gonçalves *et al.*, 2018). The data from these sensors enabled studies on UHI in the

region and surrounding areas, including methodologies with Remote Sensing (Almeida *et al.*, 2022, 2023; Gonçalves *et al.*, 2014, 2018).

2.2 Data Used and Processing Conducted

2.2.1 Satellite Images

We used Google Earth Engine (GEE) for satellite image processing, a cloud-based platform that processes data remotely, reducing the need for powerful computers and significantly minimizing processing time, which already offers a series of processed products (Hurni *et al.*, 2017; NASA, n.d.-a). We utilized the "LANDSAT/LC08/C02/T1_L2" and "LANDSAT/LC09/C02/T1_L2" collections, with overpass times around 11 AM in Bragança. These satellites operate in a nearly polar and sun-synchronous orbit at a nominal altitude of 705 km, with an orbital inclination of 98.2°, and revisit the same location every eight days, as they operate in alternating orbits, improving temporal resolution for the study areas (US Geological Survey, n.d.-a).

The thermal sensors record data at 100m, which is resampled and made available to users at 30m. In GEE, the collections are provided with atmospherically corrected surface reflectance data, and the LST is derived from the Land Surface Reflectance Code (LaSRC), generated through a single-channel algorithm developed in collaboration between the Rochester Institute of Technology (RIT) and NASA's Jet Propulsion Laboratory (JPL) (NASA, n.d.-a).

We used the code for processing LST (NASA, n.d.-b) and to filter the data for our study area between 2013 and 2024, considering only those with cloud coverage below 20%. Subsequently, we used the quality bands from each collection (QA_PIXEL) to remove pixels with clouds and cloud shadows.

We utilized the thermal band (B10) from both collections to obtain the LST. The spectral range is from 10.6 to 11.19 μm, and the data are recorded at 100m and resampled to 30m. To convert the LST to Celsius, we applied Equation (1) (NASA, n.d.-a; US Geological Survey, n.d.-b).

$$LST = TIR \times f_s + O - K \quad (1)$$

Where LST is the Land Surface Temperature (°C), TIR is the radiance in the thermal infrared band, f_s is the scale factor of Landsat 8 and 9 (0.00341802), O is the offset of Landsat 8 and 9 (149.0) and K is the conversion constant from K to °C (273.15).

To evaluate the LST by LCZs, we used a .shp file of points in GEE corresponding to the locations of the 23 sensors installed in Bragança to extract the LST values for each of them, and we added a function to export the data to a .csv file. Between 2013 and 2014, we identified 158 images, with the first date being 06/29/2013 and the last being 09/15/2024. Subsequently, we selected results where images provided data for all 23 sensors, resulting in 123 images spanning all seasons. We further filtered the data for summer and winter, obtaining 46 images for summer and 15 for winter, which were used in the processing. The lower number of winter images can be attributed to meteorological conditions, with higher cloud cover and precipitation during winter, aligning with the Köppen-Geiger classification (Barceló & Nunes, 2009).

To process and analyze the results, we calculated the SUHI by applying Equation (2), a methodology already used in other UHI studies (Almeida *et al.*, 2022; Menezes, 2017).

$$SUHI_{Int} = LST_{LCZ} - \overline{LST_{RCD}} \quad (2)$$

Where $SUHI_{Int}$ is the intensity value of the UHI at each point; LST_{LCZ} is the LST value extracted from the sensor points; and $\overline{LST_{RCD}}$ refers to the average of the LST values extracted the RCD sensors (16, 19, 20, and 23).

To present the results, we used SPSS software to create boxplots of the $SUHI_{Int}$ results, separated by LCZ and by seasonality (summer and winter), a methodology already applied in other studies (Almeida *et al.*, 2022; Saher *et al.*, 2021).

2.2.2 LST from Portable Thermal Camera

For *in situ* LST imaging, we used the HT Instruments THT33 portable thermal camera, which has a resolution of 80x80 pixels, a Field of View (FOV) of 21°x21°, a spectral range of 8 to 14 μ m, and an Instantaneous Field of View (IFOV) (@1m) of 4.53 mrad. Images were taken at a standard height of 1.5m between the camera and the target to ensure consistent operator-associated error across all samples.

The collections were conducted only on clear, cloud-free days, as these conditions affect measurement accuracy. Consequently, three data collection sessions were conducted: two in winter (02/17/2023 and 02/20/2024) and one in summer (07/27/2023). Since morning data collections had to coincide with satellite overpass times, covering all 23 points with T_a sensors was not feasible. Instead, ten representative points were selected to capture spatial

diversity and ensure at least one representative for each of the seven LCZs. The selected sensors, their respective LCZs, and the number assigned to each point for identification in the *in situ* collection are: i) CM: sensor 3, point P08; ii) CLR: sensor 6, point P07; iii) GAB: sensor 9, point P05; iv) SB: sensors 14 and 15, points P09 and P04; v) LLR: sensors 5 and 17, points P06 and P03; vi) OM: sensors 18 and 22, points P02 and P10; and vii) RCD: sensor 23, Point P01.

We assessed the diversity in LULC composition for each selected point and sampled different surfaces within a 10m radius of each sensor. We conducted two measurements at each point: i) between 10 am and 12 pm (within one hour before and after the satellite's overpass time in Bragança); and ii) between 1 pm and 3 pm to analyze temperature variability of the sampled surfaces compared to the first session. For each sampled surface, we took a photograph using a Canon EOS 800D camera to classify it afterward into the following categories: Vegetation; Exposed soil; Road with stones; Sidewalk; Asphalt; Sidewalk with shade; Asphalt with shade; Cobblestone; Iron; Curb and Vegetation with shade. Each surface is assigned a letter to differentiate its LULC for the analysis. For example, five different surfaces were collected at P01, labeled from P01A to P01E.

The HTMercury33 application was used to record, visualize, and export the LST results in .pdf format (User Manual - HTMercury33, n.d.) We created an R routine to extract specific data from the .pdf files to Excel, specifically: S (temperature associated with the fixed central cursor); H (temperature of the hottest point in the image); C (temperature of the coldest point in the image); and Mean (average temperature). Subsequently, we categorized the data by season (summer and winter) and generated boxplots with the maximum and minimum LST.

3 RESULTS AND DISCUSSION

3.1 $SUHI_{Int}$

According to Figure 3, it can be observed that the summer data exhibit greater amplitude and more outliers compared to winter data, which may be associated with a higher availability of solar radiation during this season.

In the summer, most sensors showed negative medians of $SUHI_{Int}$, except for sensors 3 (CM), 17 (LLR), and 12 (OM). In these three cases, the surroundings allowed the entry of short-wave

radiation in the early hours of the day from the east (sunrise), warming the surface in the early morning. Additionally, the structures of the OM (12) and CM (3) sensors, which contain medium-height buildings, may interfere with heat exchange with the environment due to shadow projection, making the area less prone to heat accumulation (Zheng *et al.*, 2019). In the case of LLR (17), due to the presence of heterogeneous profiles, including industrial and commercial areas and paved parking lots, heat can be absorbed, especially by elements with low albedo (pavements, structures made of cement, etc.) (Zheng *et al.*, 2019). Still in summer, the three sensors that exhibited the lowest medians consist of vegetation elements, as in the case of sensors 9 and 11 (GAB) and 15 (SB), reinforcing that the presence of vegetation aids in regulating $SUHI_{int}$ (Dai *et al.*, 2019).

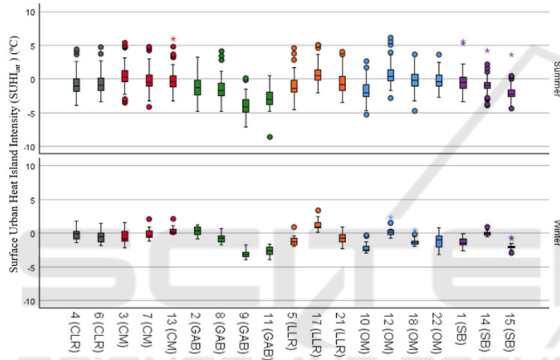


Figure 3. Boxplot illustrating the Surface Urban Heat Island Intensity ($SUHI_{int}$) across various Local Climate Zones (LCZ). The zones are categorized as follows: i) Compact Low-Rise (CLR) in gray; ii) Compact Midrise (CM) in red; iii) Urban Green Spaces (GAB) in green; iv) Large Low-Rise (LLR) in orange; v) Open Midrise (OM) in light blue; and vi) Sparsely Built (SB) in purple.

In summer, regarding higher temperatures and disregarding outliers, sensors 17 (LLR), 12, and 18 (OM) exhibited the highest values, reinforcing that the presence of anthropogenic elements may contribute to heat accumulation on the analyzed surfaces (Oke, 1987, 1988; Voogt & Oke, 2003). Finally, the lowest temperature is associated with sensor 9 (GAB), reaffirming the importance of preserving and prioritizing vegetation in spaces to regulate heat (Miles & Esau, 2020).

In winter, the medians were mainly below 0, except for sensors 13 (CM), 2 (GAB), 17 (LLR), and 12 (OM). Most of these sensors are integrated into LCZs with the presence of anthropogenic materials, converging with the values identified in summer, except for sensor 2, which contains vegetation. This

behavior can be explained by the season: in winter, vegetation enters a state of dormancy to protect itself from cooler temperatures, reducing its metabolic activities and, consequently, slowing down heat exchanges. This also limits photosynthesis, as it does in other seasons under similar conditions (Du *et al.*, 2016; French & Inamdar, 2010). There is also leaf shedding in deciduous trees, known as senescence, which may also contribute to this result (Mariën *et al.*, 2019).

As in summer, the highest temperatures are associated with sensors containing anthropogenic elements, as seen in sensors 17 (LLR), 4 and 6 (CLR), and 3 (CM). In contrast, the lowest temperatures occurred in sensors 9 and 11 (GAB), which contain vegetation (Tang *et al.*, 2017).

3.2 LST from Thermal Camera

The number of data points available in each measurement session was 220 images (110 in the morning and 110 in the afternoon) on 02/17/2023, 224 on 02/20/2024 (112 in each period), and 186 on 07/27/2023 (93 per period). The differences in sample size are attributed to occasional measurement errors related to the equipment. Figure 4 shows the recorded LST values in summer across different surfaces, with surface identification highlighted in the legend.

In general, summer temperatures are much higher than winter temperatures due to increased electromagnetic energy availability and solar angle, which minimizes shadow projection. Some surfaces reached nearly 80 °C in the morning and above 60 °C in the afternoon, mainly asphalt and exposed soil. In summer, vegetation also retains greater heat in the morning and has cooler temperatures in the afternoon. This can be explained by vegetation's prolonged exposure to electromagnetic energy in the early hours compared to built-up areas, which are shaded by structures and accumulate less heat. In the afternoon, the opposite is observed: vegetation temperatures tend to be cooler due to latent heat exchange with the environment, especially through evapotranspiration, which reduces the heating of these surfaces, in addition to the shading effect provided by tree canopies. In urban areas with low albedo surfaces, such as asphalt and concrete, the radiative balance favors the absorption of short-wavelength radiation, resulting in the surface heating of these areas (Oke, 1988; Yu *et al.*, 2019).

In a more detailed LCZ analysis, at P07 (CLR), we observe that the LULC materials such as asphalt and elements of iron, along with the lack of vegetation, contribute to higher temperatures in summer,

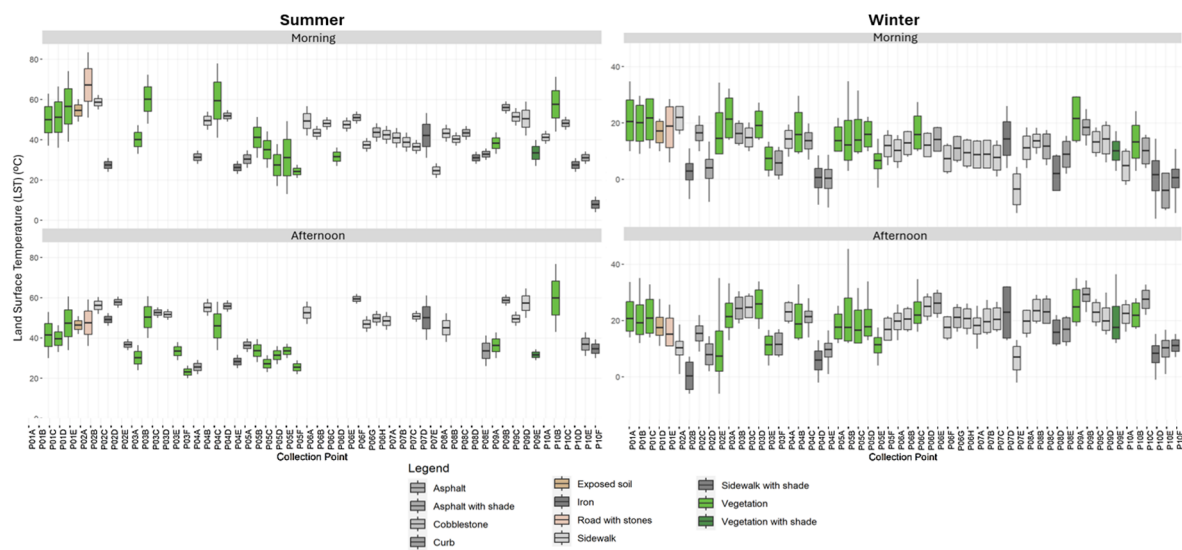


Figure 4. Boxplot of Land Surface Temperature (LST) at the ten *in situ* measurement points using a thermal camera.

particularly in the afternoon, due to the thermal inertia of these materials, which accumulate heat throughout the day. In winter, temperatures are slightly higher than most vegetation classes, especially in the afternoon (Cai *et al.*, 2017). At P08 (CM), asphalt and sidewalk temperatures were higher in summer than in winter, both in the morning and afternoon, which may be associated with the angle of electromagnetic energy. In summer, this energy is more direct, reducing shading from existing buildings in the area (Yu *et al.*, 2019).

At P05 (GAB), it is evident that vegetation created a cooler microclimate, with lower temperatures than densely built areas, especially in summer at both times of the day. The LST values for these locations are slightly lower in winter than in built-up areas, although they represent a less pronounced cooling. This could be associated with the lower radiation levels and the vegetation's dormancy process, which reduces evapotranspiration and impacts natural cooling, as discussed in the UHI_{int} results (Rose, 2019).

At points P03 and P06 (LLR), both in summer and winter, the LST showed higher values in paved areas, similar to CM and CLR points, which may be due to the lack of shading in the area. Regarding points P02 and P10 (OM), LST values in summer were more moderate, with warmer asphalt areas and cooler vegetated areas, particularly in the afternoon, potentially helping to regulate local temperature. In winter, due to lower construction density and vegetation presence, temperatures were milder at these points (Oke *et al.*, 2017).

For points P04 and P09 (SB), in both summer and winter, vegetation showed higher values in the morning, possibly due to heat accumulation in the early hours of the day, a similar effect to that observed at point P01 (RCD). The absence of large vertical barriers in open areas facilitates heat exchange with the environment in the night, promoting heat dissipation through convection. However, surface characteristics and solar radiation absorption still significantly influence daytime temperature retention in these areas. For this reason, it is suggested that UHI studies should be conducted after sunset, incorporating additional methodologies such as the use of Unmanned Aerial Vehicle (UAV), which provide greater flexibility regarding the timing of data collection.

Despite scale differences, the results were similar, with higher surface temperatures in built-up areas, reinforcing the need for mitigation measures. Incorporating vegetated surfaces in densely urbanized areas, such as green roofs and substituting impermeable surfaces with alternatives like permeable asphalt, is essential (Cai *et al.*, 2017; Gonçalves *et al.*, 2014; Mullerova & Williams, 2019). It is worth noting that, especially in summer, additional data through field visits are necessary to verify if these initial thermal behavior results are consistent across time.

4 CONCLUSIONS

This study used RS data to assess surface thermal behavior across different LCZs and identify the UHI

effect in Bragança. We utilized both satellite data and *in situ* data collected from a thermal camera, comparing the results from both techniques. In terms of spatial resolution and measurement height, the two methods differ: while Landsat is efficient for mapping larger, more homogeneous areas, the use of the thermal camera provides more detailed, localized surface data, being less influenced by atmospheric parameters and more effective at mapping heterogeneous areas. This makes the integration of these techniques particularly valuable for UHI studies.

The $SUHI_{int}$, calculated from satellite data, was higher in summer, especially in LCZs with anthropogenic surfaces, compared to those with vegetation, highlighting the influence of seasonality. *In situ* measurements corroborated these results, showing that impermeable surfaces retained more heat, particularly during summer afternoons.

The analyses suggest that integrating green areas and using high-albedo materials are strategies to mitigate the UHI effect and promote climate resilient cities. Future research could explore long-term UHI dynamics, with additional field data collection and the development of specific mitigation strategies tailored to the different LCZs in Bragança, whose findings could be applied to other urban contexts.

ACKNOWLEDGEMENTS

This work was supported by national funds through FCT/MCTES (PIDDAC): CIMO, UIDB/00690/2020 (DOI: 10.54499/UIDB/00690/2020) and UIDP/00690/2020 (DOI: 10.54499/UIDP/00690/2020); and SusTEC, LA/P/0007/2020 (DOI: 10.54499/LA/P/0007/2020). The authors are grateful to the Foundation for Science and Technology, I.P., projects UIDB/04683/2020 (<https://doi.org/10.54499/UIDB/04683/2020>), IDP/04683/2020 (<https://doi.org/10.54499/UIDP/04683/2020>). Cátia Rodrigues de Almeida was financially supported by Portuguese national funds through FCT (Grant: PRT/BD/153518/2021).

REFERENCES

- Almeida, C. R. de, Furst, L., Gonçalves, A., & Teodoro, A. C. (2022). Remote Sensing Image-Based Analysis of the Urban Heat Island Effect in Bragança, Portugal. *Environments* - *MDPI*, 9(8). <https://doi.org/10.3390/environments9080098>
- Almeida, C. R. de, Garcia, N., Campos, J. C., Alirio, J., Arenas-Castro, S., Gonçalves, A., Sillero, N., & Teodoro, A. C. (2023). Time-series analyses of land surface temperature changes with Google Earth Engine in a mountainous region. *Heliyon*, 9(8), e18846. <https://doi.org/10.1016/j.heliyon.2023.e18846>
- Almeida, C. R. de, Teodoro, A. C., & Gonçalves, A. (2021). Study of the Urban Heat Island (UHI) Using Remote Sensing Data/Techniques: A Systematic Review. *Environments*, 8(10), 105. <https://doi.org/10.3390/environments8100105>
- Barceló, A. M., & Nunes, L. F. (2009). Iberian Climate Atlas 1971-2000. In *Atlas Climático Ibérico - Iberian Climate Atlas*.
- Bragança, M. de. (n.d.). *Estratégia Municipal de Adaptação às Alterações Climáticas*. Retrieved October 1, 2024, from https://www.cm-braganca.pt/cmbraganca2020/uploads/writer_file/document/6050/B_8-Publicação_do_Plano_Municipal_de_Ambiente.pdf
- Cai, G., Liu, Y., & Du, M. (2017). Impact of the 2008 Olympic Games on urban thermal environment in Beijing, China from satellite images. *Sustainable Cities and Society*, 32, 212–225. <https://doi.org/10.1016/j.scs.2017.03.020>
- Coakley, J. A. (2003). Reflectance and Albedo, Surface. *Encyclopedia of Atmospheric Sciences*, 1914–1923. <https://doi.org/10.1016/b0-12-227090-8/00069-5>
- Dai, Z., Guldmann, J. M., & Hu, Y. (2019). Thermal impacts of greenery, water, and impervious structures in Beijing's Olympic area: A spatial regression approach. *Ecological Indicators*, 97(July 2018), 77–88. <https://doi.org/10.1016/j.ecolind.2018.09.041>
- Du, H., Song, X., Jiang, H., Kan, Z., Wang, Z., & Cai, Y. (2016). Research on the cooling island effects of water body: A case study of Shanghai, China. *Ecological Indicators*, 67, 31–38. <https://doi.org/10.1016/j.ecolind.2016.02.040>
- EPA - United States Environmental Protection Agency. (n.d.). *Ilhas de calor*. Retrieved October 13, 2024, from <http://www.epa.gov/heat-islands>
- Errea, C. L., Almeida, C. R. de, Gonçalves, A., & Teodoro, A. C. (2023). Remote Sensing Analysis of the Surface Urban Heat Island Effect in Vitoria-Gasteiz, 1985 to 2021. *Remote Sensing*, 15(12), 3110. <https://doi.org/10.3390/rs15123110>
- French, A. N., & Inamdar, A. (2010). Land cover characterization for hydrological modelling using thermal infrared emissivities. *International Journal of Remote Sensing*, 31(14), 3867–3883. <https://doi.org/10.1080/01431161.2010.483491>
- Gonçalves, A., Ornellas, G., Ribeiro, A. C., Maia, F., Rocha, A., & Feliciano, M. (2018). Urban cold and Heat Island in the City of Bragança (Portugal). *Climate*, 6(3), 1–14. <https://doi.org/10.3390/cli6030070>
- Gonçalves, A., Ribeiro, A. C., Feliciano, M., & Maia, F. (2014). *Clima Urbano de la Ciudad de Bragança*.
- Hurni, K., Heinemann, A., & Würsch, L. (2017). *Google Earth Engine Image Pre-processing Tool : Background and Methods*. 12. https://www.cde.unibe.ch/e65013/e542846/e707304/e707386/e707390/CDE_Pre-processingTool-UserGuide_eng.pdf

- Imhoff, M. L., Zhang, P., Wolfe, R. E., & Bounoua, L. (2010). Remote sensing of the urban heat island effect across biomes in the continental USA. *Remote Sensing of Environment*, 114(3), 504–513. <https://doi.org/10.1016/j.rse.2009.10.008>
- INE, I. N. de E. (n.d.). *Censos 2021*. Retrieved September 10, 2024, from https://censos.ine.pt/xportal/xmain?xpgid=censos21_main&xpid=CENSOS21&xlang=pt
- Mariën, B., Balzarolo, M., Dox, I., Leys, S., Lorène, M. J., Geron, C., Portillo-Estrada, M., AbdElgawad, H., Asard, H., & Campioli, M. (2019). Detecting the onset of autumn leaf senescence in deciduous forest trees of the temperate zone. *New Phytologist*, 224(1), 166–176. <https://doi.org/10.1111/nph.15991>
- Menezes, G. de O. (2017). *Análise do Clima Urbano da Cidade de Bragança (2012-2016): Estudo da Ilha de Calor* [Instituto Politécnico de Bragança]. <https://core.ac.uk/reader/153415740>
- Miles, V., & Esau, I. (2020). Surface urban heat islands in 57 cities across different climates in northern Fennoscandia. *Urban Climate*, 31(December 2019), 100575. <https://doi.org/10.1016/j.uclim.2019.100575>
- Mullerova, D., & Williams, M. (2019). Satellite Monitoring of Thermal Performance in Smart Urban Designs. *Remote Sensing*, 11(19), 2244. <https://doi.org/10.3390/rs11192244>
- NASA. (n.d.-a). *Earth Engine Data Catalog - Landsat*. Retrieved October 10, 2024, from <https://developers.google.com/earth-engine/datasets/catalog/landsat>
- NASA. (n.d.-b). *NASA Applied Remote Sensing Training (ARSET) program*.
- Nations, U. (n.d.). *The 17 Goals*. Retrieved October 21, 2024, from <https://sdgs.un.org/goals>
- Oke, T. R. (1982). The energetic basis of the urban heat island. *Quarterly Journal of the Royal Meteorological Society*, 108(455), 1–24. <https://doi.org/10.1002/qj.49710845502>
- Oke, T. R. (1987). *Boundary Layer Climates* (Routledge (Ed.); 2nd ed.). <http://library1.nida.ac.th/termpaper6/sd/2554/19755.pdf>
- Oke, T. R. (1988). Street design and urban canopy layer climate. *Energy and Buildings*, 11(1–3), 103–113. [https://doi.org/10.1016/0378-7788\(88\)90026-6](https://doi.org/10.1016/0378-7788(88)90026-6)
- Oke, T. R., Mills, G., Christen, A., & Voogt, J. A. (2017). *Energy Balance*. Cambridge University Press. <https://doi.org/https://doi.org/10.1017/9781139016476.007>
- ONU. (2019). World population prospects 2019. In *Department of Economic and Social Affairs. World Population Prospects 2019*. (Issue 141). <http://www.ncbi.nlm.nih.gov/pubmed/12283219>
- Pachêco, A. P. (2001). *Sensoriamento Remoto na Faixa espectral do Infravermelho termal (8 - 12 µm)*. Revista Da Comissão Brasileira de Geodésia. <https://agencia.ufpe.br/documents/39451/1778670/GEODE'SIA+online+++++2%252F2001.pdf/1a8b61d5-da8c-487e-9103-485313f03aa7>
- Rose, G. (2019). Satellite Monitoring of Thermal Performance in Smart Urban Designs. *The Routledge Companion to Urban Imaginaries, Figure 1*, 103–112. <https://doi.org/10.4324/9781315163956-8>
- Saher, R., Stephen, H., & Ahmad, S. (2021). Understanding the summertime warming in canyon and non-canyon surfaces. *Urban Climate*, 38, 100916. <https://doi.org/10.1016/j.uclim.2021.100916>
- Stewart, I. D., & Oke, T. R. (2012). Local climate zones for urban temperature studies. *Bulletin of the American Meteorological Society*, 93(12), 1879–1900. <https://doi.org/10.1175/BAMS-D-11-00019.1>
- Tang, J., Di, L., Xiao, J., Lu, D., & Zhou, Y. (2017). Impacts of land use and socioeconomic patterns on urban heat island. *International Journal of Remote Sensing*, 38(11), 3445–3465. <https://doi.org/10.1080/01431161.2017.1295485>
- US Geological Survey. (n.d.-a). *Landsat Missions*. Retrieved October 23, 2024, from <https://www.usgs.gov/landsat-missions/landsat-9>
- US Geological Survey. (n.d.-b). *Landsat Missions*. Retrieved September 12, 2024, from https://www.usgs.gov/core-science-systems/nli/landsat/landsat-8?qt-science_support_page_related_con=0#qt-science_support_page_related_con
- User manual - HTMercury33. (n.d.). Retrieved July 1, 2020, from <https://www.ht-instruments.com/en/products/mercury/download/manual/>
- Voogt, J. ., & Oke, T. . (2003). Thermal remote sensing of urban climates. *Remote Sensing of Environment*, 86(3), 370–384. [https://doi.org/10.1016/S0034-4257\(03\)00079-8](https://doi.org/10.1016/S0034-4257(03)00079-8)
- Weng, Q. (2003). Fractal analysis of satellite-detected urban heat island effect. *Photogrammetric Engineering and Remote Sensing*, 69(5), 555–566. <https://doi.org/10.14358/PERS.69.5.555>
- Weng, Q., & Fu, P. (2014). Modeling diurnal land temperature cycles over Los Angeles using downscaled GOES imagery. *ISPRS Journal of Photogrammetry and Remote Sensing*, 97, 78–88. <https://doi.org/10.1016/j.isprsjprs.2014.08.009>
- Weng, Q., Lu, D., & Schubring, J. (2004). Estimation of land surface temperature-vegetation abundance relationship for urban heat island studies. *Remote Sensing of Environment*, 89(4), 467–483. <https://doi.org/10.1016/j.rse.2003.11.005>
- Yu, K., Chen, Y., Wang, D., Chen, Z., Gong, A., & Li, J. (2019). Study of the Seasonal Effect of Building Shadows on Urban Land Surface Temperatures Based on Remote Sensing Data. *Remote Sensing*, 11(5), 497. <https://doi.org/10.3390/rs11050497>
- Zheng, H., Chen, Y., Pan, W., Cai, Y., & Chen, Z. (2019). Impact of Land Use/Land Cover Changes on the Thermal Environment in Urbanization: A Case Study of the Natural Wetlands Distribution Area in Minjiang River Estuary, China. *Polish Journal of Environmental Studies*, 28(4), 3025–3041. <https://doi.org/10.15244/pjoes/93743>
- Zhou, D., Xiao, J., Bonafoni, S., Berger, C., Deilami, K., Zhou, Y., Frolking, S., Yao, R., Qiao, Z., & Sobrino, J. A. (2019). Satellite remote sensing of surface urban heat islands: Progress, challenges, and perspectives. *Remote Sensing*, 11(1), 1–36. <https://doi.org/10.3390/rs11010048>